Synthesis and Screen Printing of Dopant Free Nano-crystalline SnO₂ (101) Thick Film for Gas Sensor Application

Anil D. Garje[1],*, Manoj Mayaji Ovhal[1,2], Shweta Mishra[1], Namrata Bagwe[1]

[1]Department of Physics, Sir Parashurambhau College, Pune 411030, Maharashtra, India
[2]Flexible and Printable Electronics, Jeonbuk National University, Jeonju, South Korea

*Corresponding author: E-mail: adgarje@gmail.com

Nano-crystalline tin (II) oxide (SnO₂) was successfully synthesized by a simple and cost-effective surfactant assisted solution precipitation technique. The structural, optical, and morphological characterization of as synthesized nano-crystalline SnO₂ was confirmed by X-Ray diffraction (XRD), ultraviolet-visible (UV-Vis) spectroscopy, and transmission electron microscopy (TEM). The nano-crystalline SnO₂ possesses tetragonal lattice structure (rutile phase) with preferential growth along (101) plane and average crystallite size of 8 ±2 nm were confirmed by XRD Rietveld refinement. The TEM images were showed quasi spherical particles with average particle size of 10 ±2 nm. The optical energy band gap of 3.76 eV confirms the electronic conduction mechanism in SnO₂. Furthermore, the synthesized nano-crystalline SnO₂ with 15 wt % glass frit was used as a functional material to fabricate thick film sensors using cost-effective screen printing method. The sensor shows high sensitivity towards H₂, CO, and LPG selectively at optimal operating temperatures of 120, 150 and 70°C respectively for 100 ppm concentration of each gas. The improvement in sensitivity, selectivity, and stability at low operating temperature and their correlation with the nano-crystalline SnO₂ (101) plane, small particle size and optical band gap were also envisaged along with repeatability, reproducibility, calibration, and aging effect.

Introduction

Increased in air pollution with the regular use of hazardous, flammable, and toxic gases (such as hydrogen (H₂), carbon monoxide (CO), nitrous oxide (NO), sulfur dioxide (SO₂), ozone (O₃), ammonia (NH₃), and liquid petroleum gas (LPG)) in industries creating a threat to environmental deterioration by many folds in past few decades. The presence of these gases in the surrounding air causes respiratory problems in animals (including human) and plants. Also, fire explosion in residences or companies were constantly damaging Earth's environment. Cost of pollution/gases detection equipment and their stable sensing performance at lower operating temperature are key challenges in the sensor industry. To detect measure and monitor the concentration of hazardous gases, advance gas sensors with high performance active material and low fabrication cost are required. The most important parameters of gas sensors are sensitivity, selectivity and stability at low optimal operating temperature; a) sensitivity is the response to small concentration of pollutants, b) selectivity is the strong response to only one pollutant, negligible for others, and c) stability is the signal reproducibility over the period of time [1-6]. Researchers have successfully developed a metal oxide semiconductor (MOS) sensor for the detection of volatile organic compounds (VOCs) which are of great importance in many applications involving either control of hazardous chemicals or noninvasive diagnosis [7]. The semiconductor oxide such as tin di oxide (SnO₂), zinc oxide (ZnO), titanium di oxide (TiO₂), and iron oxide (Fe₂O₃) based gas sensors has been widely used as domestic and industrial gas detectors for gas-leak alarm, process control, and pollution control [8-9]. The sensitivity of the semiconductor oxide sensors is directly depending upon the surface to volume ratio of particles. The increase in surface to volume ratio is responsible for improvement in the redox reaction sites with these target gas molecules and is resulting in higher conductivity. Among all others semiconductor oxide sensors, nano-crystalline SnO₂ have been observed to be a potential candidate for high performance gas sensing material. It shows high reactivity towards reducing gases at relatively low operating temperatures [10], due to its naturally stable non-stoichiometry property [11]. Moreover, nano-crystalline SnO₂ was easily synthesized by using low-cost solution precipitation technique [12]. Researchers were successfully attempted to control the particle size of SnO₂ using stabilizers such as surfactants, polymers, ligands, and dendrimers. These were usually incorporated during the synthesis process [1-10]. Xu *et. al.,* were studied the effect of SnO₂ particle size on gas sensitivity. The average particle size of SnO₂ below 20 nm

Advanced Materials Letters
www.vbripress.com/aml

IAAM®
Advancement of Materials to Global Excellence
www.iaamonline.com

were significantly improves the sensitivity toward reducing gases [13-16]. The high optimal operating temperature is one of the key problems for SnO_2 based gas sensors as it consumes high power. The crystal structural and exposing crystal plane to pollutants are playing a crucial role in decreasing an optimal operating temperature. As, the reaction temperature of surface adsorbed oxygen (O_2^-) is different at different SnO_2 Miller planes [17-19]. Therefore, many attempts have been focused on creating defects (by adding dopant) in SnO_2 crystal structure. The defects not only improve selectivity, sensitivity, and response time of sensors but also affect the optimal operating temperature of sensors [20]. Henceforth the nano-crystalline SnO_2 gas sensor exiting with controlled particle size distribution and direction growth along its Miller plane without dopants might be helpful for high sensitivity, selectivity, and stability of the gas sensor at low optimal operating temperature. Furthermore, the fabrication processes were significantly affecting the sensing performance. Though, the printing methods such as gravure, slot-die, screen, and 3D direct writing were benefits as simplified processing steps, reduce material wastage, high throughput, easy patterning, and low fabrication cost for the futuristic flexible and smart sensors [21-22]. The formulated semiconductor paste with good rheological properties was used in printing method by controlling the printing parameter. The screen printing method is easy and compatible with roll-to-roll printing [21]. Thus, the simple, low-cost surfactant-assisted solution precipitation method for synthesis of nano-crystalline SnO_2 along with screen printing method for fabrication of thick film sensors are suitable for industrial purpose.

This work reports synthesis of dopant free +surfactant-assisted nano-crystalline SnO_2 using simple and low-cost solution precipitation technique. The nano-crystalline SnO_2 exhibits tetragonal structure (rutile phase) with directional growth along the (101) Miller plane and average crystallite size of 8 ± 2 nm. The optical properties and morphology of the SnO_2 nano-crystals were confirmed by ultraviolet-visible (UV-Vis) spectroscopy and transmission electron microscope (TEM), respectively. Further, the simple and cost-effective screen-printing method was opted to fabricate nano-crystalline SnO_2 thick film sensors. The prepared sensors were showed the best response towards H_2, CO, and LPG gas at lower optimal operating temperatures of 120, 150 and 70ºC respectively. The reproducibility, repeatability, and stability of the sensors at low optimal operating temperature were envisaged.

Experimental

Materials

Tin chloride dihydrate ($SnCl_2.2H_2O$), sodium dodecyl sulphate (SDS), ammonia (NH_3), lead borosilicate glass frit, ethyl cellulose (EC), butyl carbetol acetate (BCA). Deionized water was used throughout the synthesis.

Synthesis of nano-crystalline SnO₂

0.1 M $SnCl_2.2H_2O$ was mixed with optimized 50 wt. % of anionic surfactant SDS in deionized water. After 2 hours of stirring, NH_3 solution was added drop wise till the pH 9. The final solution was kept stirring for 2 hours.

The chemical reaction involved in the formation of SnO_2 is shown Equation (1)

$$SnCl_2.2H_2O + H_2O + 4NH_3 \rightarrow SnO_2 + 2HCl \uparrow + 4NH_4 \uparrow \quad (1)$$
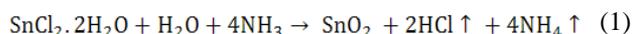
The precipitate was filtered and washed repeatedly using deionized water to remove the residual of chloride ions. The obtained gel precipitate was dried at 50 ºC under IR lamp. Finally, the dried gel was crushed by using agate mortar and pestle to acquired smooth powder like texture. Annealing of synthesized SnO_2 powder was done at optimized 450 ºC for 45 minutes and further used for fabrication of thick film sensors.

Fabrication of thick film sensors

Thick film sensors were fabricated using screen printing technique. Schematic synthesis and fabrication method for thick film planar sensor is illustrated in **Fig. 1**. The formulated paste contains synthesized nano-crystalline SnO_2 powder along with optimized 15 wt % lead borosilicate glass frit. The prepared paste was used as a functional material for the screen-printing purpose. EC and BCA were added as a temporary binder to get thixotropic property to the paste. The solid to liquid ratio was maintained as 70:30. The 96% pure alumina substrates of size 10 mm × 20 mm were used as base for the thick film sensors. The formulated SnO_2 paste was printed in desired pattern on these alumina substrates. These printed samples were dried under IR lamp for 20 minutes followed by firing at 525 ºC for 45 minutes in a muffle furnace. Electrical contacts were made using silver paste and were helpful for further characterization of samples. Thickness of the samples was measured by using a light section microscope (Carizeisss Jena, Model Bk 70_50, Carl Zeiss, Jena, Germany).
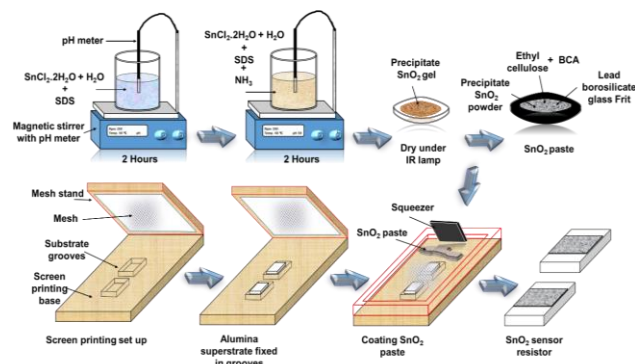
Fig. 1. Schematic representation of synthesis and fabrication method of nano-crystalline SnO_2 sensor.

Advanced Materials Letters
www.vbripress.com/aml

IAAM®
Advancement of Materials
to Global Excellence
www.iaamonline.com

Characterizations techniques

Structural characterization

As synthesized surfactant-assisted nano crystalline SnO_2 was characterized by X-ray diffraction (XRD, Bruker D8 advanced diffractometer) in the scanning range (2 theta) of 20°–80° with the step size of 0.02° using Cu-Kα radiations of wavelength 1.54 Å. The Rietveld refinement of XRD data have been done by using FULLPROF program. The morphological characteristic was studied using TEM micrograph

Optical charecterization

Optical characterization was carried out by using UV-Vis spectrometer in the rage 200 nm to 800 nm.
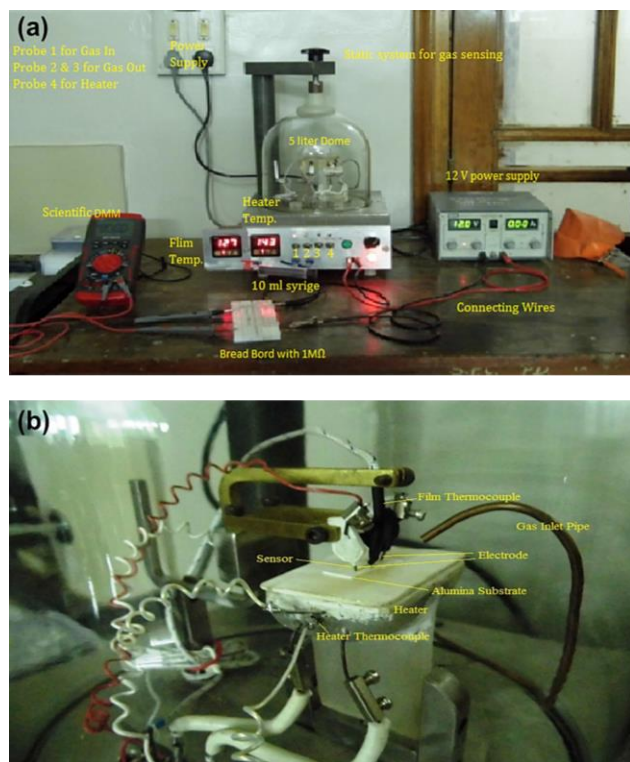
Fig. 2. (a) Static gas sensing set up, (b) SnO_2 gas sensor with heater and measurement electrodes.

Sensor characterization

The sensor characterization was done on a static system under laboratory conditions (controlled 40% RH). The volume of gas chamber is 5 litres. The temperature of the sensor was varied from 25ºC to 250ºC using a resistive heater and measured on a chromel–alumel thermocouple. The sensitivity factor (%) was defined as ''$S\ (\%) = G_{gas}/G_{air} \times 100$'' where G_{gas} and G_{air} are the conductance of the sensor in the presence and absence of H_2, CO and LPG gas in air, respectively [23]. The DC measurements were done by the standard two-probe method. **Fig. 2** represents the static gas sensing set up used for the gas sensing measurement. Reproducibility of results was checked typically for four times. Optimal temperature of the sensor is defined as the temperature at which the sensor shows maximum change in the conductance due to the presence of the test gas [**24**]. Repeatability of all gas sensors was checked for the gas concentration of 100 PPM each. The response time is defined as the time taken for the sensor to reach from 10 % to 90 % of the saturation value of the sensitivity after the surface has come in contact with the test gas. The response time of the sensors was measured by injecting 400 ppm volume of gas inside the chamber; at the optimal temperature of respective gas. For measuring recovery time, the sensor was exposed to air ambient by maintaining the optimal temperature constant and then the time was noted till it achieves at least 90 % of its original value. Calibration of the sensors was carried out by keeping the sensor at the optimal temperature of the particular gas and concentration of the gas was varied from 10 to 1000 ppm. The schematic representation of gas sensing mechanism in nanocrystalline SnO_2 based sensors is expressed in **Fig. 3**.
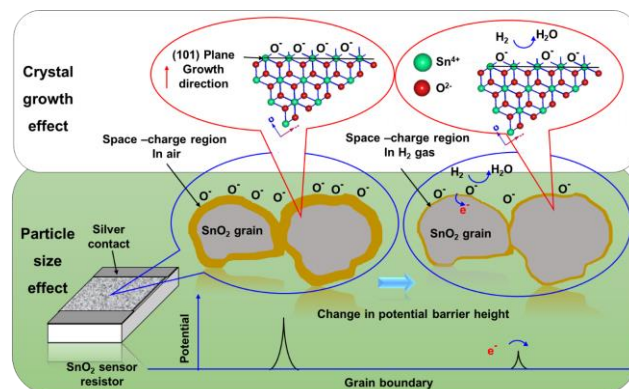
Fig. 3. Schematic representation of gas sensing mechanism in nano-crystalline SnO_2 sensors with the effect of particles size and crystal growth along (101) Miller plane.
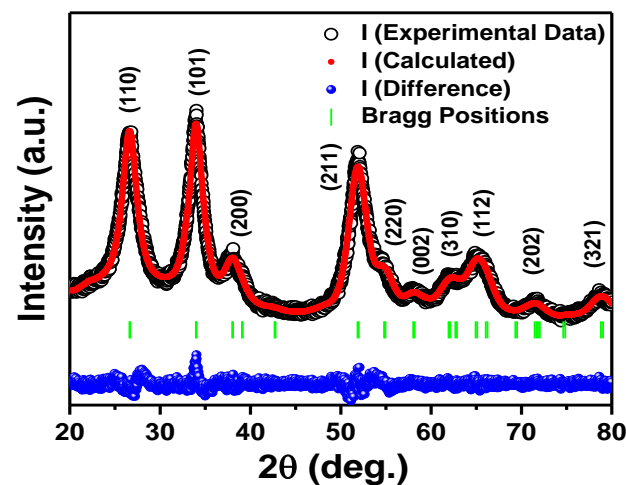
Fig. 4. Rietveld refinement of nano-crystalline SnO_2 powder.

Results and discussion

Crystal structure and Rietveld analysis

The XRD pattern and Rietveld refinement of surfactant assisted nano-crystalline SnO_2 is shown in **Fig. 4**. XRD pattern of surfactant assisted nano-crystalline SnO_2 was

Advanced Materials Letters
www.vbripress.com/aml

IAAM®
Advancement of Materials to Global Excellence
www.iaamonline.com

exhibited stronger reflection for (110), (101), (200), (211), (220), (002), (310), (112), (202), and (321) Miller planes in well agreement with JCPDS Card No. 41-1445. The nano-crystalline SnO_2 was showed a unique (101) direction growth compare to the standard SnO_2. The preferential growth direction and texture coefficient (CT) was calculated by relative high intensity diffraction peaks. CT calculated from XRD analysis of as synthesized SnO_2 for (101) Miller plane was 1.11, which was higher than the standard CT of 0.96 as given in the JCPDS card No. 00-41-1445. The XRD pattern of surfactant assisted nano-crystalline SnO_2 was refined by Rietveld refinement using FULLPROF Suite programme using space group of P 42/m n m (136) with preferred orientation of along (101) plane. All the peaks were well fitted with lowest chi² (χ^2) as 1.10. Auto generated crystallographic information file (.CIF) was represent the lattice parameter a = 4.72 ±1 Å and c = 3.18 ±2 Å and was showing atomic positions of 'Sn' and 'O' arranged in tetragonal crystal structure as shown in **Fig. 5**. The average crystallite size (D) was calculated using Debye-Scherrer formula [**25**];

$$D = \frac{0.9 \times \lambda}{\beta \times Cos\,\theta} \quad (2)$$

where, λ is a wavelength of Cu Kα radiation of 1.54 Å, and β is full width of the diffraction peak at the half maximum (FWHM) at Bragg diffraction angle 2θ. The average crystallite size of as synthesized nano-crystalline SnO_2 was found to be 8 ±2 nm. Theoretically, nano-crystalline SnO_2 with (101) surface possesses higher and stable surface energy than (110) and (100) surfaces [**26**]. This (101) surface significantly were found to influence the gas sensing properties of the SnO_2 [**18**].
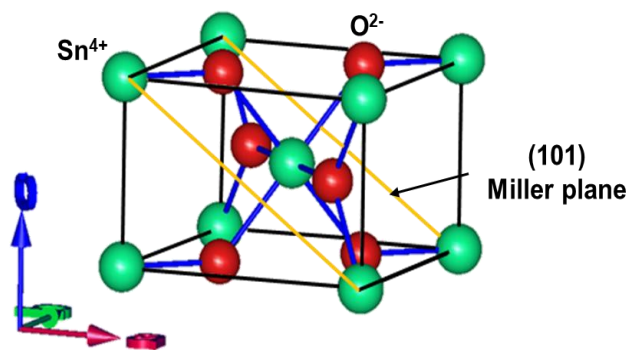
Fig. 5. Tetragonal rutile SnO_2 with (101) Miller plane graphic generated using CIF file.

Optical properties

The optical bad gap (E_g) of synthesized nano-crystalline SnO_2 was evaluated using UV visible absorption spectroscopy as shown in **Fig. 6**. The 'E_g' of the nano-crystalline SnO_2 was determined by applying the Tauc model in the absorption region [**27**];

$$(\alpha h\nu)^2 = A(h\nu - E_g) \quad (3)$$

where, 'A' is a constant for direct transition, 'hʋ' is incident photon energy, 'E_g' is the energy band gap, and 'h' is the Planks constant in eV. The 'E_g' was obtained by extrapolating the linear portion of $(\alpha h\nu)^2$ to the photon energy 'hʋ' axis. The value of the optical band gap was elucidating as 3.76 eV [**27**]. The increase in band gap was related to direct bandgap as the crystal growth along (101) direction [**26**]. By the addition of 50 wt % SDS surfactant, the optical absorption edge was slightly shifted towards shorter wavelength, which was also attributed to the decrease in particle size.
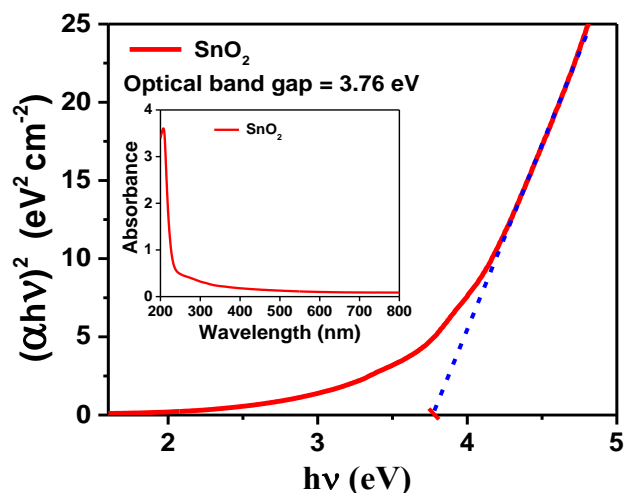
Fig. 6. Toac plot of the nano-crystalline SnO_2 powder (in inset UV-Visible absorption spectra of nano-crystalline SnO_2 powder).

Morphological studies

The TEM micrograph as shows in **Fig. 7** confirms the presence of quasi spherical nano particles.
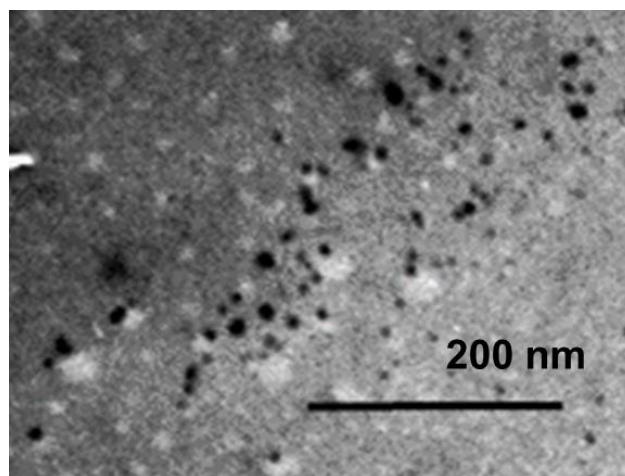
Fig. 7. TEM micrograph of synthesized nano-crystalline SnO_2 powder.

Furthermore, to calculate average particle size, the TEM micrograph was analyzed using ImageJ software. The average particle size distribution using histogram plot is presented in **Fig. 8**.

Advanced Materials Letters
www.vbripress.com/aml

IAAM®
Advancement of Materials
to Global Excellence
www.iaamonline.com
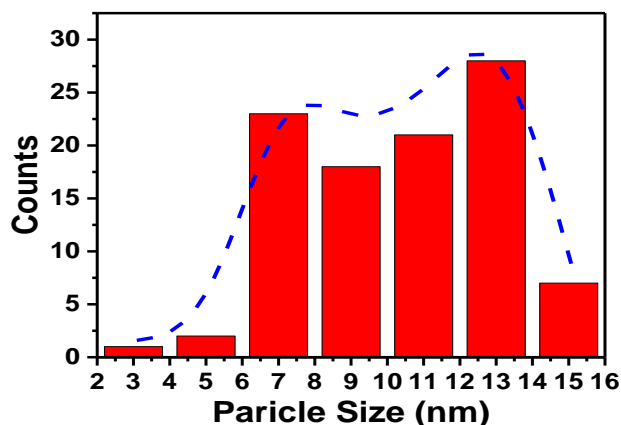
Fig. 8. Histogram plot of nano-crystalline SnO_2 particle size from TEM micrograph.

The lower crystallite size in XRD might be because of line broadening effect as compared with the average particle size observed in TEM. The selected area electron diffraction (SAED) patterns of nano-crystalline SnO_2 as represented in **Fig. 9** verifies the continuous rings indexed to the (110), (101), (200), and (211) Miller planes of the tetragonal structure of SnO_2. These rings were in well agreement with the high intensity peaks observed in the XRD spectra. It confirms the polydispersity and nano-crystalline nature of as synthesized nano-crystalline SnO_2.
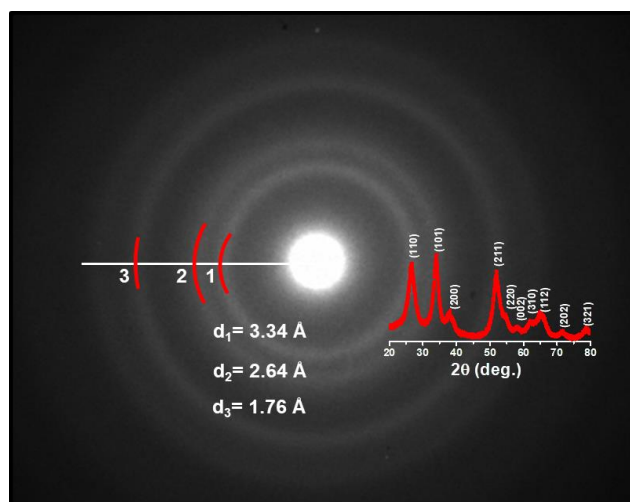
Fig. 9. SAED pattern of nano-crystalline SnO_2 powder, merge with XRD spectra and high intensity diffraction peak with respective inter planar distance (d_1-d_3).

Gas sensing performance of the sensor

The H_2, CO and LPG sensing performance of the sensor are presented in figure 10 **(a)**.

H_2 sensor performance

For H_2 sensor, the sensitivity factor was increased with temperature and reaches to a maximum value of 3008 at 120ºC as depicted in **Fig. 10(a)**. The increase and decrease in the sensitivity factor was observed in the graph, indicates the phenomenon of adsorption and desorption of

the gas on sensor surface. The reactions taking place between the surface adsorbed oxygen and H_2 gas molecular species is as follows,

$$O^-_{(ads)} + H_2 \rightarrow H_2O + e^-_{(cb)} \qquad (4)$$
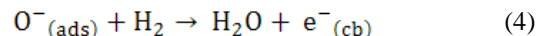
The nano-crystalline SnO_2 in the resistor was connected to their neighbors either by grain boundaries or potential barrier height (neck). The conduction electrons were moved through a channel penetrating each potential barrier, which was normally formed by connecting the pores between the two neighboring grains. Therefore, the diameter and length of the potential barrier was depended on the size of the grain and its aperture being attenuated by the strength of the surface-charge density. Similar trend had been observed elsewhere [28-30]. The repeatability of fabricated using nano-crystalline SnO_2 sensors of average thickness ~ 30 ±3 μm were tested at 100 ppm of H_2 and their performance was presented in figure 10(b) It was observed that H_2 sensors shows good response at 120 ± 9 ºC and variation in S_f in the range of ± 6 % only. The surfactant assisted nano-crystalline SnO_2 based sensors were showed 2 times higher sensitivity towards H_2 than the sensors fabricated by SnO_2 synthesized without using surfactant [23].

CO sensor performance

The fabricated sensors shows good response towards CO gas at operating temperature of 150ºC along with sensitivity factor of 2572 as illustrated in figure10(a). The reaction between the CO gas molecules and the surface adsorbed oxygen species is as follows;

$$O^-_{(surf)} + CO_{(gas)} \rightarrow CO_2 + or\ e^-_{(cb)} \qquad (5)$$
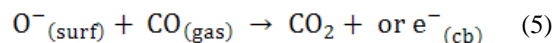
The repeatability of fabricated SnO_2 sensors for CO (100 ppm) is rendered in **Fig. 10(c)**. It was observed that, the operating temperature of fabricated SnO_2 sensor for CO sensing shows variation in the range of about ±11 ºC and variation in S_f(%) was observed in the rage of ±10 % only.
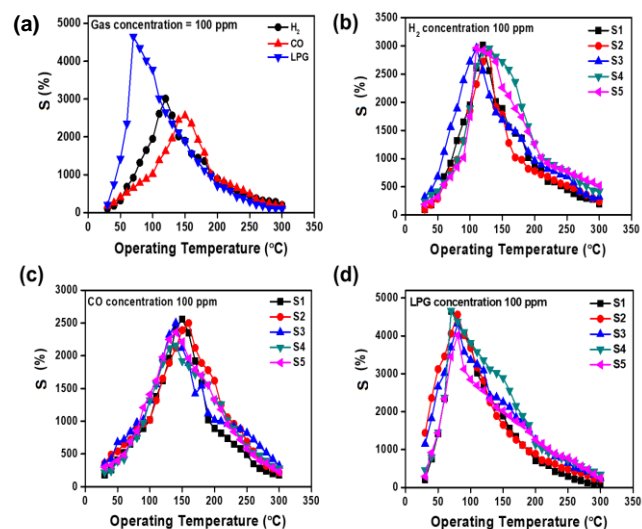
Fig. 10. (a) Sensing performance of the H_2, CO, and LPG sensor. Repeatability of the (b) H_2, (c) CO and (d) LPG sensors.

LPG sensor performance

The LPG sensor performance were unveiled the operating temperature of 70ºC along with sensitivity factor of 4660. However, the reaction mechanism for LPG is quite complex and proceeds through several intermediate steps, which are not yet fully understood [**31,32**]. It is well known, that the LPG is a mixture of CH_4, C_3H_8 and C_4H_{10}. These molecules with reducing hydrogen species are bound to carbon atoms. The overall reaction of LPG molecules with adsorbed oxygen is explained as,

$$C_nH_{2n+2} + 2O^- \leftrightarrow H_2O + C_nH_{2n} - O + e^-_{(cb)} \quad (6)$$
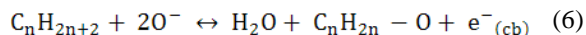
where, C_nH_{2n+2} represent the methane (CH_4), propane (C_3H_8), and butane (C_4H_{10}). The repeatability of fabricated nano-crystalline SnO_2 based sensor for LPG sensing performance against 100 ppm concentration was checked and is presented in **Fig. 10(d)**. It was observed that, the operating temperature showed variation in the range of about ±70 ºC and variation in S_f (%) is of ±8 % only. The surfactant assisted nano-crystalline SnO_2 based sensors were showed 5 times higher sensitivity towards LPG than the sensors fabricated by SnO_2 synthesized without using surfactant [**6,19**]. The optimal temperature is different for different gases. Responses against other gases with and without surfactants are presented in **Table 1**.

Table 1. Responses against other gases with and without surfactants.

Sensor	% S (with surfactant)	%S (without surfactant)	Reference
H_2	3008	1500	[23]
CO	2572	2500	[23]
LPG	4660	825	[6,19]

Table 2. Selectivity of H_2, CO and LPG sensors at optimal temperature.

Detecting Gases	S_f (%)	Operating Temp. (ºC)	Response time (s)	Recovery time (s)	Selectivity	
H_2	3008	120	12	84	H_2/CO 1.8	H_2/LPG 1.14
CO	2572	150	16	34	CO/H_2 1.36	CO/LPG 1.4
LPG	4619	70	10	36	LPG/H_2 4.89	LPG/CO 6.95
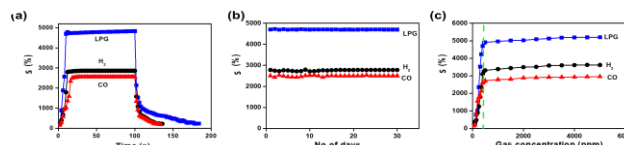
Fig. 11. (a) Response and recovery time, (b) aging effect and (c) calibration for H_2, CO, and LPG sensors.

Based on this analysis, the sensor fabricated using nano-crystalline SnO_2 was showed better selectivity for LPG over H_2 and CO at relatively lower optimal operating temperature of 70 ºC. At the operating temperature of 150 ºC, sensors showed moderate selectivity for CO over LPG, but lesser for H_2. The selectivity of sensors at their optimal operating temperatures is presented in **Table 2**. The response time was ~12s, 16s, and 10s, whereas the recovery time was nearly 84s, 34s, and 36s for H_2, CO, and LPG, respectively as presented in **Fig. 11(a)**. The aging effect or stability of the sensors was elucidated by investigating the response to H_2, CO, and LPG at 100 ppm for one month and illustrated in **Fig. 11(b)**. The measurement shows lesser stable during initial 12 days for CO and H_2. Later, the performance of fabricated sensors was found to be consistent around the optimum value with a variation of less than ± 1%. The calibration curves of nano-crystalline SnO_2 sensors as presented in **Fig. 11(c)** showed three regions, as region I; from 10-100 ppm,

Table 3. Comparative study on the sensitivity and selectivity of SnO_2 based sensors.

Fabrication process	Composition	Morphology	plane	Gas	Gas conc. (PPM)	Operating temp. (ºC)	Sensor response	Res. time/ recovery time (sec.)	Ref.
Thermal evaporation	SnO_2	Nanorod	101	H_2	1000	300	$(R_g - R_a)/R_a \times 100\% = 3.4$	--	[3]
Co-precipitation	SnO_2	Spherical	--	CO	10	95	$R_a/R_g = 16$	--	[10]
Thermal evaporation	SnO_2	Nanowire	110	H_2	1000	300	$(R_g - R_a)/R_a \times 100\% = 1.7$	--	[36]
Microwave assisted	SnO_2	Nano structure	110	LPG	500	250	$R_g - R_a)/R_a \times 100\% = 78$	9 / 15	[37]
Microwave assisted	SnO_2	Irregular spherical	110	LPG	1000	250	$R_a/R_g = 10$	9 / 22	[38]
Microwave assisted	SnO_2	Irregular spherical	110	LPG	600	300	$R_a/R_g = 5$	--	[39]
Electrospinning	Pd coted SnO_2	Irregular spherical	101	H_2	100	160	$R_a/R_g = 28$	--	[42]
Electrospinning	SnO_2 doped InO_3	Nanowires	--	CO	100	200	$(R_g - R_a)/R_a \times 100\% = 17$	30 / 30	[40]
Co-precipitation	(Cu+Ce)–doped SnO_2	Irregular spherical	110	LPG	100	250	$(R_g - R_a)/R_a \times 100\% = 30$	--	[41]
Co-precipitation	SnO_2	Irregular spherical	101	H_2	400	120	$R_a/R_g = 30$	12 / 84	this work
				CO	400	150	$R_a/R_g = 25$	16 / 34	
				LPG	400	70	$R_a/R_g = 46$	10 / 36	

Advanced Materials Letters
www.vbripress.com/aml

IAAM®
Advancement of Materials to Global Excellence
www.iaamonline.com

region II; from 100 to 400 ppm, and region III; from 400-5000 ppm. The sensitivity factor in region II is higher than region I and III. Similar regions in calibration curve are reported in literature [33-35]. The comparison of SnO_2 sensing performance to the recent literatures were depicted in **Table 3** [36-42].

Role of surfactant

This increase in sensitivity was attributed to the role of SDS surfactant for controlling the particle size of SnO_2 particles. The nano-crystalline SnO_2 particles were isolated by the SDS surfactant, which was provided restriction on the growth of grain boundaries. Interestingly, the addition of SDS surfactant was affected to directional growth along (101) Millar plane, which was rich in oxygen vacancies and was responsible for enhanced in gas sensitivity at low optimal temperature. The surfactant assisted nano-crystalline SnO_2 adsorbed oxygen present in air at its surface sites because of its natural stable non-stoichiometry property [34]. The surface sites along (101) Miller plane was showed higher and stable surface energy than the Miller planes in tetragonal SnO_2 structure [26]. The high sensitivity and selectivity of the nano-crystalline SnO_2 based sensors is attributed to the addition of surfactant. This was responsible for controlling the particle size at around 10 ± 2 nm and was providing high surface area and higher oxygen vacancies due to the crystal growth along (101) plane, as shown in figure 3.

Conclusions

The dopant free surfactant-assisted nano-crystalline SnO_2 powder was synthesized by simple and low-cost solution precipitation technique. The effect of surfactant on crystal structure, particle size, and optical band gap was studied. The cost-effective screen-printing method was opted to fabricate nano-crystalline SnO_2 sensors. The sensors were selective towards H_2, CO, and LPG gas at low operating temperatures of 120, 150, and 70ºC respectively. The selectivity and high sensitivity of the sensors was attributed to the addition of surfactant, which was responsible for low particle size, high surface to volume ratio, and higher oxygen vacancies due to SnO_2 crystal preferential growth along (101) Miller plane.

References

1. Marcus, Y.; Encyclopedia of Applied Electro Chemistry, Springer, NY, **2014**.
2. Leite, E.R.; Weber, I.T, Longo, E., Varela, J. A.; *Adv. Mater,* **2000**, *12,* 965.
3. Wang, B.; Zhu L.F.;Yang Y.H.; Xu N.S.; ang G.W.; *J. Phys. Chem. C.* **2008**, *112,* 6643.
4. Choi, Y. J.; Hwang, I.; Park, J. G.; Choi, K. J.; Park, J.; Lee, J.; *Nanotechnology,* **2008**, *190,* 955.
5. Rsan, N.B.; Weimar, U.; *J. Phys. Condens. Matter.,* **2003**, *15,* 813.
6. Dey, A.; *Mater. Sci. Eng. B Solid-State Mater. Adv. Technol.,* **2018**, *229,* 206.
7. Sun, Y. F.; Liu, S. B.; Meng, F. L.; Liu, J. Y.; Jin, Z.; Kong, L.T.; Liu, J. H.; *Sensors,* **2012**, *12,* 2610.
8. Eranna, G.; Joshi, B.C.; Runthala, D.P.; Gupta, R.P.; *Solid State Mater Sci.,* **2004**, *29,* 111.
9. Akbar, S.; Dutta, P.; Lee, C.; *Int. J. Appl. Ceram. Technol.,* **2006**, *3,* 302.
10. Hermida, D.P.; Wiranto, G.; Hiskia, Nopriyanti R.; *J. Phys. Conf. Ser.,* **2016**, *776,* 012061.
11. Batzill, M.; Chaka, A.M.; Diebold, U.; *Europhys Lett.,* **2004**, *65,* 61.
12. Niu, M.; Huang, F.; Cui, L.; Huang, P.; Yu, Y.; Wang, Y.; *ACS Nano.,* **2010**, *4,* 681.
13. Yamazoe, N., Sakai, G.; Shimanoe, K.; Catalysis Surveys from Asia, **2003**, *7,* 63.
14. Jana, N.R.; Gearheart, L.; Murphy, C.J.; *Adv. Mater.,* **2001**, *13,* 1389.
15. Dixit, S.G.; Mahadeshwar, A.R.; Haram, S.K.; *Colloids Surfaces Eng. Asp.,* **1998**, *133,* 69.
16. Vidyasagar, C.C.; Arthoba, Naik; *Arab. J. Chem.,* **2016**, *9,* 507.
17. Oviedo, J.; Gillan, M.J.; *Surf. Sci.,* **2000**, *463,* 93.
18. Katsiev, K.; Batzill, M.; Boatner, L.A.; Diebold, U.; *Surf. Sci.,* **2008**, *602,* 1699.
19. Wang, C.; Yin, L.; Zhang, L.; Xiang, D.; Gao, R.; *Sensors,* **2010**, *10,* 2088.
20. Ridha, N.J.; Jumali, M.H.H.; Umar, A.A.; Alosfur, F.; *Int. J. Electrochem. Sci.,* **2013**, *8,* 4583.
21. Khan, S.; Lorenzelli, L.; Dahiya, R.S.; *IEEE Sens. J.,* **2015**, *15,* 3164.
22. Lewis, J.A.; Gratson, G.M.; *Mater. Today,* **2004**, *7,* 32.
23. Garje, A.D.; Aiyer, R.C.; *Int. J. Appl. Ceram. Tech.,* **2007**, *4,* 446.
24. Dayan, N.J.; Sainkar, S.; Karekar, R.; Aiyer, R.; *Thin Solid Films,* **1998**, *325,* 254.
25. Robertson, J.H.; *Acta Crystallogr. Sect. A.,* **1979**, *35,* 350.
26. Floriano, E.A.; Scalvi, L.V. de A.; Sambrano, J.R.; Geraldo, V.; *Mater. Res.,* **2010**, 13, 437.
27. Gu, F.; ang S.F.; Lü, M.K.; Zhou, G.J.; Xu, D.; Yuan, D.R.; *J. Phys. Chem. B.,* **2004**, *108,* 8119.
28. Xu, C.; Tamaki, J.; Miura, N.; Yamazoe, N.; *Sensors Actuators B Chem,* **1991**, *3,* 147.
29. Mishra, V.N.; Agarwal, R.P.; *Microelectronics J.;* **1998**, *29,* 861.
30. Wang, X.; Yee, S.S.; Carey, W.P.; *Sensors Actuators B Chem.,* **1995**, *25,* 454.
31. Choudhary, S.; Annapoorni, S.; Malik, R.; *Sensors and Actuators A Phys.,* **2019**, *293,* 207.
32. Kumar, M.; Bhatt, V.; Abhyankar, A.C.; Kim, J.; Kumar, A.; Patil, S.H.; Yun, J.; *Sci, Rep.,* **2018**, 1.
33. Dayan, N.J.; Karekar, R.N.; Aiyer, R.C.; *J. Mat Sci: Mat in Ele.,* **1997**, *8,* 277.
34. Batzill, M.; *Sensors,* **2006**, *6,* 1345.
35. Kumar, M.; Kumar, A.; Abhyankar, A.C.; *Ceram. Int.,* **2014**, *40,* 8411.
36. Thomas, B.; Deepa, S.; Prasanna, Kumari K.; Ionics (Kiel), **2019**, *25,* 809.
37. Thomas, B.; Prasanna, Kumari K.; Deepa, S.; *Sensors Actuators, A Phys.,* **2020**, *301,* 111755.
38. Srivastava, A.; Lakshmikumar, S.; Rashmi, K.; Jain, K, *Sens Actuat B Chem.,* **2007**, *126,* 583.
39. Onkar, S.G.; Raghuwanshi, F.C.; Patil, D.R.; Krishnakumar T.; *Mater. Today Proc.,* **2020**, *23,* 190.
40. Hsu, K.C.; Fang, T.H.; Tang, I.T.; Hsiao, Y.J.; Chen, C.Y.; *J. Alloys Compd,* **2020**, 822.
41. Bagal K.N., Bagal L.K., Mulla I.S., Suryavanshi S.S, Ceram. Int., **2012**, *38,* 4835.
42. Wang, F.; Hu, K.; Liu, H.; Zhao, Q.; Wang, K.; Zhang, Y.; *Int. J. Hydrogen Energy,* **2020**, *45,* 7234.